SPICE-Based Circuit Analysis of Power Flow Coupling Effect in Double-Input Cuk–Buck DC–DC Converters

Hao Zhang, *Member, IEEE*, Jiao Gao, Chuanzhi Yi, Dachu Dong, and Feng Zheng, *Member, IEEE*

***Abstract*—An equivalent simulation program with integrated circuit emphasis (SPICE) based circuit is derived from the proposed small-signal averaged model of double-input Cuk–Buck dc–dc converter so that the power flow coupling effect amongst input/output ports is easy to be analyzed in terms of circuit theory rather than pure mathematics. Based on the equivalent SPICE-based circuit, common mode and differential mode power flow decomposition is presented to unveil the power flow coupling between three ports, and furthermore benefits frequency response analysis. It is shown that common mode perturbation analysis reveals the power flow coupling amongst input and output ports, whereas differential mode perturbation analysis does the power flow coupling between input ports. Meanwhile, the explanation of circuit knowledge is provided for power flow coupling effect. Particularly, it is found that the occurrence of the pseudo resonant phenomenon is the result of counteract effect of the common mode and differential mode components in power mismatched condition. Besides, the application of frequency-selective decoupling is proposed to weaken the power flow coupling between ports. Finally, theoretical analysis is verified by experimental ones. These results are useful to understand coupling effects in multiple-input converters and provide a guidance to the controller optimization and engineering application.**

***Index Terms*—Common mode, coupling effect, differential mode, double-input dc–dc converter, frequency-selective decoupling, power flow, resonance, simulation program with integrated circuit emphasis (SPICE) based circuit.**

Manuscript received July 3, 2021; revised October 26, 2021; accepted October 31, 2021. Date of publication November 4, 2021; date of current version December 31, 2021. This work was supported in part by the Natural Science Basic Research Plan in Shaanxi Province of China under Grant 2021JM-014 and in part by the National Natural Science Foundation of China under Grant 51577141. Recommended for publication by Associate Editor T. Mishima. *(Corresponding author: Hao Zhang.)*

Hao Zhang and Jiao Gao are with the State Key Lab of Electrical Insulation and Power Equipment, School of Electrical Engineering, Xi'an Jiaotong University, Xi'an 710049, China (e-mail: haozhang@xjtu.edu.cn; jiaogao@stu.xjtu.edu.cn).

Chuanzhi Yi is with the State Key Lab of Electrical Insulation and Power Equipment, School of Electrical Engineering, Xi'an Jiaotong University, Xi'an 710049, China, and also with Bosch Automotive Product (Suzhou) Co., Ltd., Suzhou 215000, China (e-mail: yichuanzhi@stu.xjtu.edu.cn).

Dachu Dong is with the State Key Lab of Electrical Insulation and Power Equipment, School of Electrical Engineering, Xi'an Jiaotong University, Xi'an 710049, China, and also with the Hangzhou Power Supply Company of State Grid Zhejiang Electric Power Co., Ltd., Hangzhou 310000, China (e-mail: xjtuddc@stu.xjtu.edu.cn).

Feng Zheng is with the School of Electrical and Mechanical Engineering, Xidian University, Xi'an 710071, China (e-mail: f.zheng@mail.xidian.edu.cn).

Color versions of one or more figures in this article are available at https://doi.org/10.1109/TPEL.2021.3125035.

Digital Object Identifier 10.1109/TPEL.2021.3125035

I. Introduction

THE increasing attraction of renewable energy promotes the development of power conversion technologies for such resources in the past decades [1], [2]. Due to the intermittency and volatility of the renewable sources such as wind and solar, they are usually artificially connected to harness the full power generation capacity and maintain the continuous power supply for the load [3]. This transpires the development of multiple-input converters (MICs), which combine several standalone power converters for various power sources into one single power stage with integrated multiple input ports. Owing to the advantages of less components, lower cost, more compact size and better dynamic performance, various kinds of multiple-input converter have been proposed for different power conversion applications in those past years [4]–[6].

Due to the requests of low cost and compact size in MICs, the input ports must share a common output buffer to transfer power to the load simultaneously. Therefore, all the input ports are coupled with each other via the output buffer, and MICs present many unmanageable features such as richer topology, more diverse operating modes and more complex coupling effects due to the interaction between the input ports, which undoubtedly poses a great challenge to the modeling, analysis and design of such converters [7]–[10]. In order to meet the increasingly demanding requirements for the power management and better dynamic performance, together with system coupling analysis, many researchers have devoted themselves into the design of decoupled control methods [11]–[13]. Decoupling matrix is an effective method to deal with the coupling effect of control loops, which transforms the original transfer function matrix into a diagonal matrix. As a result, the coupling effect of the system can be suppressed and the regulators can be designed independently [14], [15]. Nonlinear adaptive controllers such as one-cycle controller and Lyapunov-based nonlinear controller are also practical solutions to simplify the design procedure of the controller for MICs, which adaptively against disturbances of the state variables and improve the dynamic response [16]–[18]. Moreover, an improved switching strategy is presented in [19] to transform an MIC into an equivalent single-input single-output system for analysis, which simplifies controller design and implementation. However, the previous mentioned works till relies on those abstract mathematical models so that the explanation of circuit knowledge is rarely provided for power flow coupling

effect, e.g., pseudo resonant frequency occurs. This becomes a barrier for guiding the controller optimization and engineering application.

During the operation of the MIC, the system inevitably suffers from a great variety of disturbances, e.g., input source harmonic perturbation. During these processes, the system may be subject to overvoltage, overcurrent, and complex nonlinear behaviors, which leads to the increase of device stress and the shortening of device lifetime. Moreover, harmonics perturbation may cause local parallel resonant or series resonant, which will amplify the harmonics, greatly aggravate the harm, and even cause serious accidents. Particularly, compared with the single-input single-output (SISO) converters, MICs always emerge more special resonant points within half-switching frequency [20]–[22]. These resonant points may lead to drastic variations in frequency response and greatly affecting the electromagnetic interference levels of the system [23], which may threaten the stability and reliability of the converter and even making the system collapse. Unfortunately, although the frequency response of MICs is obtained only by numerical methods in many previous works, the analysis of resonant points has not been reported yet.

In general, the presence of a resonant point implies that the coupling degree of some energy storage elements increases rapidly, which causes a dramatic change in the direction or magnitude of some specific power flows in the system. Unlike SISO converters, the MICs (such as double-input converters) consist of at least two input sources, i.e., there may exists power flow from one input port to another during some disturbance, which may generate an equivalent circulating current from one input port to the other [24]. The circulating current is frequently observed in modular multilevel converter (MMC), which is caused by variations of arm capacitor voltages [25], [26]. The orthogonal decomposition and the equivalent circuit model are effective ways to explore the mechanism of the circulating current [27]. Interestingly, regarding each arm as an independent voltage source, the structure of MMC is similar with that of the MICs, which is of important reference value in the analysis of the coupling effect of input ports in MICs. Therefore, it is of great significance to find a way to explore the power flow coupling effect in MICs from the view of circuit knowledge.

Taking the double-input Cuk–Buck dc–dc converter as an example, the power flow decomposition method will be employed to explore the physical mechanism of power flow coupling amongst input/output ports. The rest of this article is organized as follows. Section II will illustrate the system description. Then, the equivalent simulation program with integrated circuit emphasis (SPICE) based circuit of the converter will be derived from the proposed small-signal averaged model and the power matched condition will be given. In Section III, first, based on the equivalent SPICE-based circuit, the common mode and differential mode decomposition will be proposed to perform frequency response analysis. Furthermore, the resonant points and coupling characteristics with respect to system parameters will be obtained. Besides, the mismatched condition is discussed, and the mechanism of the pseudo resonant will be provided. In Section IV, the application of frequency-selective decoupling will be introduced to realize the decoupling at the resonant points. Some experimental results will be performed to verify the theoretical and numerical ones in Section V. Finally, Section VI concludes this article.

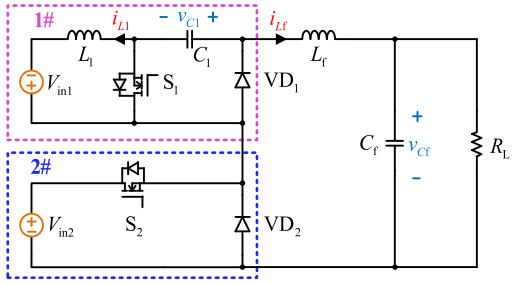

Fig. 1. Schematic diagram of the double-input Cuk–Buck dc–dc converter.

II. System Description and SPICE-Based Circuit

A. System Description

The power stage of the double-input Cuk–Buck dc–dc converter is shown in Fig. 1. The Cuk-type input port $1^{\#}$ consists of a power MOSFET S_1, a diode VD_1, an inductor L_1 and a capacitor C_1 in order that the output voltage can expand to a wide range, i.e., both step-up and step-down voltage of the input voltage $V_{\rm in1}$ can be obtained. The Buck-type input port $2^{\#}$ is composed of a power MOSFET S_2 and a diode VD_2 so that it can only provide step-down voltage. The two voltage source ports transfer the input power to the load resistor $R_{\rm L}$ separately or simultaneously via the shared voltage output buffer, which contains the inductor $L_{\rm f}$ and the capacitor $C_{\rm f}$. Here, let both L_1 and $L_{\rm f}$ operate under continuous conduction mode, and all the components are assumed to be ideal, then S_1 (S_2) and VD_1 (VD_2) turn ON and OFF complementarily. Therefore, four possible circuit topological configurations will exist within one switching period, the detailed differential equations of each topological mode are given as follows.

Configuration 1: S_1 is ON, VD_1 is OFF, S_2 is ON and VD_2 is OFF

$$\begin{cases} \frac{{\rm d}i_{L1}}{{\rm d}t} = \frac{1}{L_1}V_{\rm in1} \\ \frac{{\rm d}i_{Lf}}{{\rm d}t} = \frac{1}{L_{\rm f}}v_{C1} - \frac{1}{L_{\rm f}}v_{C\rm f} + \frac{1}{L_{\rm f}}V_{\rm in2} \\ \frac{{\rm d}v_{C1}}{{\rm d}t} = -\frac{1}{C_1}i_{Lf} \\ \frac{{\rm d}v_{C\rm f}}{{\rm d}t} = \frac{1}{C_{\rm f}}i_{Lf} - \frac{1}{C_{\rm f}R_{\rm L}}v_{C\rm f}\ . \end{cases} \tag{1}$$

Configuration 2: S_1 is ON, VD_1 is OFF, S_2 is OFF and VD_2 is ON

$$\begin{cases} \frac{{\rm d}i_{L1}}{{\rm d}t} = \frac{1}{L_1}V_{\rm in1} \\ \frac{{\rm d}i_{Lf}}{{\rm d}t} = \frac{1}{L_{\rm f}}v_{C1} - \frac{1}{L_{\rm f}}v_{C\rm f} \\ \frac{{\rm d}v_{C1}}{{\rm d}t} = -\frac{1}{C_1}i_{Lf} \\ \frac{{\rm d}v_{C\rm f}}{{\rm d}t} = \frac{1}{C_{\rm f}}i_{Lf} - \frac{1}{C_{\rm f}R_{\rm L}}v_{C\rm f}\ . \end{cases} \tag{2}$$

Configuration 3: S_1 is OFF, VD_1 is ON, S_2 is ON and VD_2 is OFF

$$\begin{cases} \frac{{\rm d}i_{L1}}{{\rm d}t} = -\frac{1}{L_1}v_{C1} + \frac{1}{L_1}V_{\rm in1} \\ \frac{{\rm d}i_{Lf}}{{\rm d}t} = -\frac{1}{L_{\rm f}}v_{C\rm f} + \frac{1}{L_{\rm f}}V_{\rm in2} \\ \frac{{\rm d}v_{C1}}{{\rm d}t} = \frac{1}{C_1}i_{L1} \\ \frac{{\rm d}v_{C\rm f}}{{\rm d}t} = \frac{1}{C_{\rm f}}i_{Lf} - \frac{1}{C_{\rm f}R_{\rm L}}v_{C\rm f}\ . \end{cases} \tag{3}$$

Configuration 4: S_1 is OFF, VD_1 is ON, S_2 is OFF and VD_2 is ON

$$\begin{cases} \frac{\mathrm{d}i_{L1}}{\mathrm{d}t} = -\frac{1}{L_1}v_{C1} + \frac{1}{L_1}V_{\mathrm{in1}} \\ \frac{\mathrm{d}i_{Lf}}{\mathrm{d}t} = -\frac{1}{L_\mathrm{f}}v_{C\mathrm{f}} \\ \frac{\mathrm{d}v_{C1}}{\mathrm{d}t} = \frac{1}{C_1}i_{L1} \\ \frac{\mathrm{d}v_{C\mathrm{f}}}{\mathrm{d}t} = \frac{1}{C_\mathrm{f}}i_{L\mathrm{f}} - \frac{1}{C_\mathrm{f}R_\mathrm{L}}v_{C\mathrm{f}}\ . \end{cases} \tag{4}$$

The main purpose of this article is to explore the coupling effect of power flow from each input source on the system, in which the low frequency power flow usually plays a major role in system dynamics as well as stability. Therefore, the state-space averaging method is applied to capture the low frequency power flow information. The averaged model of the power stage is obtained as

$$\begin{cases} \frac{\mathrm{d}i_{L1}}{\mathrm{d}t} = -\frac{(1-d_1)}{L_1}v_{C1} + \frac{1}{L_1}V_{\mathrm{in1}} \\ \frac{\mathrm{d}i_{Lf}}{\mathrm{d}t} = \frac{d_1}{L_\mathrm{f}}v_{C1} - \frac{1}{L_\mathrm{f}}v_{C\mathrm{f}} + \frac{d_2}{L_\mathrm{f}}V_{\mathrm{in2}} \\ \frac{\mathrm{d}v_{C1}}{\mathrm{d}t} = \frac{1-d_1}{C_1}i_{L1} - \frac{d_1}{C_1}i_{Lf} \\ \frac{\mathrm{d}v_{C\mathrm{f}}}{\mathrm{d}t} = \frac{1}{C_\mathrm{f}}i_{L\mathrm{f}} - \frac{1}{C_\mathrm{f}R_\mathrm{L}}v_{C\mathrm{f}} \end{cases} \tag{5}$$

where d_1 and d_2 are the duty cycles of the switches S_1 and S_2, respectively.

B. Small-Signal SPICE-Based Circuit

In practical applications, SPICE models are usually used in power electronics analysis, e.g., core loss estimation and radiated susceptibility analysis [28], [29]. In order to investigate the underlying mechanism of power flow coupling effect, i.e., in what way power flow couple amongst three ports including two input ports and one output port, an equivalent SPICE-based circuit is derived from the small-signal averaged model including some abstract mathematical expressions. In other word, the equivalent SPICE-based circuit is the visual form of the abstract averaged model so that the power flow coupling effect amongst three ports is easy to be analyzed in terms of circuit theory rather than pure mathematics. In what follows, a small-signal model and the corresponding equivalent SPICE-based circuit will be obtained so as to analyze the power flow coupling of the double-input Cuk–Buck converter.

Suppose that the system works in the stable operating point $[I_{L1}, I_{Lf}, V_{C1}, V_{Cf}]$, then small perturbation will act on the state variables, duty cycles and the input voltages in the neighborhood of the operating point according to small-signal approach. Consequently, based on the proposed averaged model (5), the small-signal representation can be obtained as

$$\begin{cases} \frac{\mathrm{d}\hat{i}_{L1}}{\mathrm{d}t} = -\frac{D_1{}'}{L_1}\hat{v}_{C1} + \frac{V_{C1}}{L_1}\hat{d}_1 + \frac{1}{L_1}\hat{V}_{\mathrm{in1}} \\ \frac{\mathrm{d}\hat{i}_{Lf}}{\mathrm{d}t} = \frac{D_1}{L_\mathrm{f}}\hat{v}_{C1} - \frac{1}{L_\mathrm{f}}\hat{v}_{C\mathrm{f}} + \frac{V_{C1}}{L_\mathrm{f}}\hat{d}_1 + \frac{V_{in2}}{L_\mathrm{f}}\hat{d}_2 + \frac{D_2}{L_\mathrm{f}}\hat{V}_{\mathrm{in2}} \\ \frac{\mathrm{d}\hat{v}_{C1}}{\mathrm{d}t} = \frac{D_1{}'}{C_1}\hat{i}_{L1} - \frac{D_1}{C_1}\hat{i}_{Lf} - \frac{I_{L1}+I_{L2}}{C_1}\hat{d}_1 \\ \frac{\mathrm{d}\hat{v}_{C\mathrm{f}}}{\mathrm{d}t} = \frac{1}{C_\mathrm{f}}\hat{i}_{L\mathrm{f}} - \frac{1}{R_\mathrm{L}C_\mathrm{f}}\hat{v}_{C\mathrm{f}} \end{cases} \tag{6}$$

where D_1 and D_2 are the steady-state duty cycles, and $D_1{}' = 1 - D_1$.

Although more accurate models are available in the literature [30], it is assumed here that all circuit components are considered to be ideal. From the proposed small-signal model (6), the equivalent SPICE-based circuit with controlled sources can be obtained as Fig. 2.

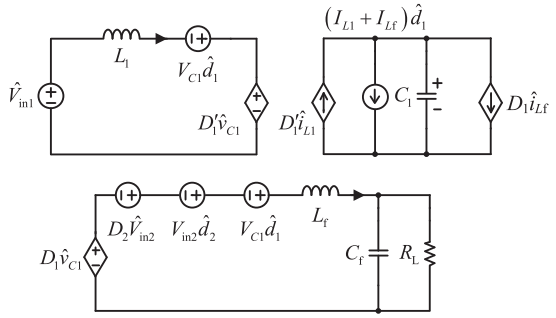

Fig. 2. Equivalent SPICE-based circuit with controlled sources.

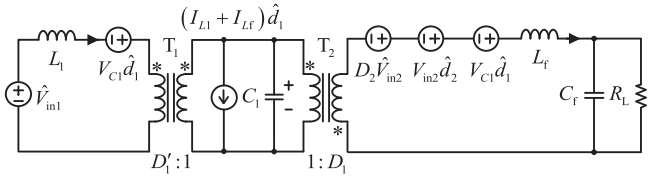

Fig. 3. Equivalent SPICE-based circuit with ideal transformers from the small-signal model (6).

However, the equivalent SPICE-based circuit divides the components of the system into three independent loops, which becomes a barrier of system analysis. Noted that the controlled source can be substituted by the ideal transformer in some manner, so the equivalent SPICE-based circuit can be transformed into the corresponding circuit with ideal transformers (see Fig. 3).

As far as the power flow coupling is concerned, the effect of the duty cycle perturbations should not be considered in the double-input converter under study. Accordingly, rearrange (6) and it gives

$$\begin{bmatrix} \frac{\mathrm{d}\hat{i}_{L1}}{\mathrm{d}t} \\ \frac{\mathrm{d}\hat{i}_{Lf}}{\mathrm{d}t} \\ \frac{\mathrm{d}\hat{v}_{C1}}{\mathrm{d}t} \\ \frac{\mathrm{d}\hat{v}_{C\mathrm{f}}}{\mathrm{d}t} \end{bmatrix} = \begin{bmatrix} 0 & 0 & -\frac{D_1{}'}{L_1} & 0 \\ 0 & 0 & \frac{D_1}{L_\mathrm{f}} & -\frac{1}{L_\mathrm{f}} \\ \frac{D_1{}'}{C_1} & -\frac{D_1}{C_1} & 0 & 0 \\ 0 & \frac{1}{C_\mathrm{f}} & 0 & -\frac{1}{R_\mathrm{L}C_\mathrm{f}} \end{bmatrix} \begin{bmatrix} \hat{i}_{L1} \\ \hat{i}_{Lf} \\ \hat{v}_{C1} \\ \hat{v}_{C\mathrm{f}} \end{bmatrix} + \begin{bmatrix} \frac{1}{L_1} & 0 \\ 0 & \frac{D_2}{L_\mathrm{f}} \\ 0 & 0 \\ 0 & 0 \end{bmatrix} \begin{bmatrix} \hat{V}_{\mathrm{in1}} \\ \hat{V}_{\mathrm{in2}} \end{bmatrix}. \tag{7}$$

And then the corresponding equivalent SPICE-based circuit is illustrated in Fig. 4.

From Fig. 4, one can obtain the following power balance relation:

$$\hat{v}_{\mathrm{in1}}I_{L1} + \hat{v}_{L1}I_{L1} + V_{C1}\hat{i}_{C1} + \hat{v}_{Lf}I_{Lf} + V_{C\mathrm{f}}\hat{i}_{C\mathrm{f}} + V_{C\mathrm{f}}\hat{i}_{R\mathrm{L}} + D_2\hat{v}_{\mathrm{in2}}I_{Lf} = 0. \tag{8}$$

Provided that the power flow perturbations from the two input sources are the same, then the following expression will be

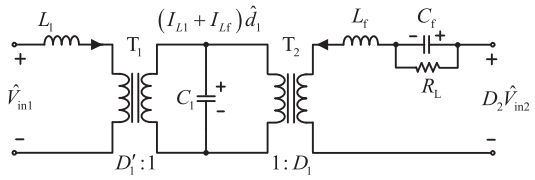

Fig. 4. Equivalent SPICE-based circuit with ideal transformers from the small-signal model (7).

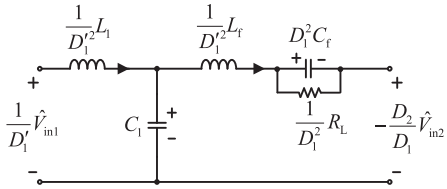

Fig. 5. Equivalent SPICE-based circuit.

satisfied:

$$|\hat{v}_{\mathrm{in}1}I_{L1}| = |D_2\hat{v}_{\mathrm{in}2}I_{Lf}|\,. \tag{9}$$

By simplifying (9), the power matched condition will be given in the following expression:

$$D_2 = \frac{D_1}{1-D_1}. \tag{10}$$

Noted that under the matched condition the strong coupling effect between the two input ports exists in the double-input converters.

Since the four windings of the two ideal transformers existing in the above SPICE-based circuit leads to some difficulty in the power flow coupling analysis, how to convert the SPICE circuit to one simpler equivalent circuit becomes of great significance. From the equivalent SPICE-based circuit in Fig. 4, it can be found that the capacitor C_1 is only one bridge between the input port $1^{\#}$ and the input port $2^{\#}$. That is, C_1 plays the key role in double-input Cuk–Buck converter. Thus, all the impedances can be transferred from the primary side of the transformer T_1 and the secondary side of the transformer T_2 to C_1 side, and then the equivalent SPICE-based circuit is obtained, as depicted in Fig. 5. Noted that since the two ideal transformers have opposite dotted terminals, the two input ports are opposite in Fig. 5. Therefore, the power flow perturbations of the two input sources are also opposite.

III. Power Flow Coupling Analysis

As is mentioned previously, the well-known frequency response approach is widely adopted in a great variety of circuit systems, but it cannot be applied to MICs straightly. Fortunately, common mode and differential mode decomposition analysis is found to be one effective and powerful method of system signal flow so that power flow in MICs can be surely unveiled by using this decomposition method. Hence, the common mode and differential mode decomposition will be applied to the double-input Cuk–Buck converter.

A. Preliminaries of Common Mode and Differential Mode Decomposition in MICs

For MICs, the common mode component can be expressed as the average of the *N* port perturbations. However, the difference between every two port perturbations can derive a differential mode component, so the generalized differential mode components are much more than the generalized common mode component.

Provided that the *N* input port perturbations of the multiple-input converter are formulated as $\hat{V}_{\mathrm{in}(k)}(k=1\sim N)$, respectively. Then, there exists only one common mode component of *N* port perturbations in the multiple-input system, which is defined as the average of *N* input port perturbations, namely

$$\hat{V}_{\mathrm{com}} = \frac{1}{N}\sum_{k=1}^{N}\hat{V}_{\mathrm{in}(k)}. \tag{11}$$

The *N* port differential mode component can be defined as the average of the difference between two of the *N* input perturbations. Obviously, there are C_N^2 differential mode components at port *N*, and each differential mode component can be given as

$$\begin{cases} \hat{V}_{\mathrm{dif}(1)(2)} = \frac{1}{N}\left(\hat{V}_{\mathrm{in}1} - \hat{V}_{\mathrm{in}2}\right) \\ \hat{V}_{\mathrm{dif}(1)(3)} = \frac{1}{N}\left(\hat{V}_{\mathrm{in}1} - \hat{V}_{\mathrm{in}3}\right) \\ \quad\vdots \\ \hat{V}_{\mathrm{dif}(j)(k)} = \frac{1}{N}\left(\hat{V}_{\mathrm{in}(j)} - \hat{V}_{\mathrm{in}(k)}\right)(1 \le j < k \le N) \\ \quad\vdots \\ \hat{V}_{\mathrm{dif}(N-1)(N)} = \frac{1}{N}\left(\hat{V}_{\mathrm{in}(N-1)} - \hat{V}_{\mathrm{in}(N)}\right)\,. \end{cases} \tag{12}$$

As for the double-input Cuk–Buck converter, the common mode and differential mode decomposition of input port power flow perturbation can be defined as

$$\begin{bmatrix} \hat{V}_{\mathrm{com}} \\ \hat{V}_{\mathrm{dif}} \end{bmatrix} = \begin{bmatrix} \frac{1}{2} & \frac{1}{2} \\ \frac{1}{2} & -\frac{1}{2} \end{bmatrix} \begin{bmatrix} \hat{V}_{\mathrm{in}1} \\ \hat{V}_{\mathrm{in}2} \end{bmatrix} \tag{13}$$

where $\hat{V}_{\mathrm{com}}$ and $\hat{V}_{\mathrm{dif}}$ are the common mode and differential mode components, respectively.

Appling (13) into (7), then, the following common mode and differential mode perturbation equation will be derived as:

$$\begin{bmatrix} \frac{\mathrm{d}\hat{i}_{L1}}{\mathrm{d}t} \\ \frac{\mathrm{d}\hat{i}_{Lf}}{\mathrm{d}t} \\ \frac{\mathrm{d}\hat{v}_{C1}}{\mathrm{d}t} \\ \frac{\mathrm{d}\hat{v}_{Cf}}{\mathrm{d}t} \end{bmatrix} = \begin{bmatrix} 0 & 0 & -\frac{D_1'}{L_1} & 0 \\ 0 & 0 & \frac{D_1}{L_f} & -\frac{1}{L_f} \\ \frac{D_1'}{C_1} & -\frac{D_1}{C_1} & 0 & 0 \\ 0 & \frac{1}{C_f} & 0 & -\frac{1}{R_L C_f} \end{bmatrix} \begin{bmatrix} \hat{i}_{L1} \\ \hat{i}_{Lf} \\ \hat{v}_{C1} \\ \hat{v}_{Cf} \end{bmatrix} + \begin{bmatrix} \frac{1}{L_1} & \frac{1}{L_1} \\ \frac{D_2}{L_f} & -\frac{D_2}{L_f} \\ 0 & 0 \\ 0 & 0 \end{bmatrix} \begin{bmatrix} \hat{V}_{\mathrm{com}} \\ \hat{V}_{\mathrm{diff}} \end{bmatrix}. \tag{14}$$

Since both the common mode and differential mode components are too abstract, the equivalent SPICE-based circuits have to be translated in terms of the common mode and differential mode perturbation (14). Furthermore, with the help of equivalent SPICE-based circuits, the power flow transmission

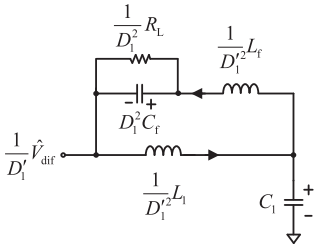

Fig. 6. Equivalent SPICE-based circuit under differential mode perturbation.

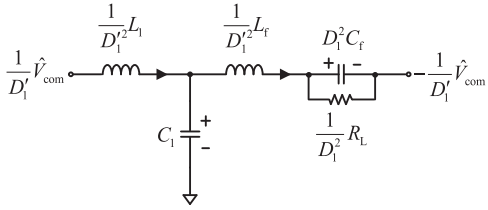

Fig. 7. Equivalent SPICE-based circuit under common mode perturbation.

paths under common mode and differential mode perturbations can be clearly identified to verify the power flow coupling amongst three ports more convincingly. In this following, the power flow coupling of the double-input system will be analyzed according to two cases, i.e., power matched condition and power mismatched condition.

B. Under Power Matched Condition

1) Differential Mode Perturbation Analysis: With differential mode power flow perturbations, the perturbation directions of input ports in Fig. 5 are the same. Interestingly, due to the constraints of power matched condition (10), the perturbation amplitudes of the input ports are the same, namely

$$\frac{1}{D'_1}\hat{V}_{\text{in1}} = \frac{D_2}{D_1}\hat{V}_{\text{in2}}. \tag{15}$$

Since the differential mode component $\hat{V}_{\text{dif}} = \frac{1}{2}(\hat{V}_{\text{in1}} - \hat{V}_{\text{in2}})$ is zero, the equivalent SPICE-based circuit can be further translated under the differential mode perturbation, which is shown in Fig. 6. The equivalent SPICE-based circuit will be analyzed from low, intermediate, and high frequency domain, respectively.

In low frequency domain, C_1 and C_{f} are equivalent to open circuit while L_1 and L_{f} are regarded as short circuit, so there exists no power flow amongst three ports. Therefore, the amplitudes of all the state variables except v_{C1} are zero. In addition, i_{L1} increases at a rate of 20 dB/dec in low frequency domain while $i_{L\text{f}}$ and $v_{C\text{f}}$ have a slope of 40 dB/dec.

In high frequency domain, C_1 and C_{f} are equivalent to short circuit while L_1 and L_{f} are regarded as open circuit, so there is no power flow amongst three ports. Likewise, i_{L1} and $i_{L\text{f}}$ decrease at a rate of –20 dB/dec in high frequency domain while v_{C1} and $v_{C\text{f}}$ have a slope of –40 dB/dec.

In intermediate frequency domain, the coupling degree of some energy storage elements at the resonant frequency increases sharply, which leads to drastic changes in the direction or magnitude of some specific power flows in the system. According to the structure of the equivalent SPICE-based circuit in Fig. 6, the resonant frequency of the SPICE-based circuit under differential mode perturbation is discussed from two aspects, as follows.

If the impedance of R_{L} is much smaller than the impedance of C_{f}, i.e., C_{f} is negligible, the resonant frequency of the SPICE circuit under differential mode perturbation is given as

$$f_{\text{dif0}} = \frac{1}{2\pi\sqrt{\left(\frac{1}{D_1'^2}L_1 \parallel \frac{1}{D_1^2}L_{\text{f}}\right)C_1}} = \frac{1}{2\pi}\sqrt{\frac{D_1^2L_1 + D_1'^2L_{\text{f}}}{L_1L_{\text{f}}C_1}}. \tag{16}$$

On the other hand, if the impedance of R_{L} is much higher than that of C_{f}, i.e., R_{L} is negligible and it is regarded as open circuit. Thus, two resonant frequencies of the SPICE-based circuit under differential mode perturbation are originated from L_1, L_{f}, C_1, and C_{f}, which can be expressed as

$$f_{\text{dif1}} = \frac{1}{2\pi}\sqrt{\frac{a_2 - \sqrt{a_2^2 - 4a_1}}{2a_1}}$$
$$f_{\text{dif2}} = \frac{1}{2\pi}\sqrt{\frac{a_2 + \sqrt{a_2^2 - 4a_1}}{2a_1}} \tag{17}$$

where $a_1 = \frac{1}{D_1'^2}L_1L_{\text{f}}C_1C_{\text{f}}$ and $a_2 = \frac{1}{D_1'^2}L_1C_1 + \frac{D_1^2}{D_1'^2}L_1C_{\text{f}} + L_{\text{f}}C_{\text{f}}$.

2) Common Mode Perturbation Analysis: Based on the form of common mode perturbation $\hat{V}_{\text{com}} = \frac{1}{2}(\hat{V}_{\text{in1}} + \hat{V}_{\text{in2}})$, the equivalent SPICE-based circuit under the common mode perturbation is depicted in Fig. 7.

Similarly, the low-frequency and high-frequency characteristics of each state variables can be acquired. In low frequency domain, C_1 and C_{f} are equivalent to open circuit while L_1 and L_{f} are regarded as short circuit, so power only flows from the input port 1# into the input port 2#. Thus, i_{L1}, $i_{L\text{f}}$, and $v_{C\text{f}}$ depend on the load R_{L} while v_{C1}does $\frac{1}{D'_1}$. In high frequency domain, C_1 and C_{f} are equivalent to short circuit while L_1 and L_{f} are regarded as open circuit, so there exists no power flow amongst three ports.

If compared with Figs. 6 and 7 in intermediate frequency domain, one power flow transmission path under common mode perturbation is the same as differential mode perturbation. Different from the differential mode perturbation, the power flow under the common mode perturbation has the other transmission path. This implies the power flow coupling between ports becomes more complicated.

Due to the existence of the same transmission path, there exists the same resonant frequency under common mode perturbation as differential mode perturbation, which can be expressed as

$$f_{\text{com0}} = f_{\text{dif0}} \text{ or } \begin{cases} f_{\text{com1}} = f_{\text{dif1}} \\ f_{\text{com2}} = f_{\text{dif2}} \end{cases} \tag{18}$$

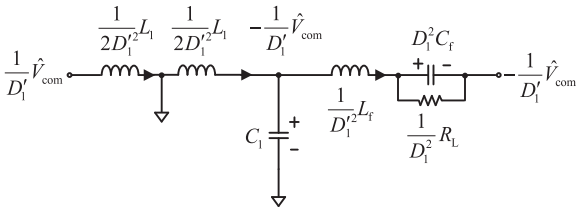

Fig. 8. Equivalent SPICE-based circuit in parallel resonant.

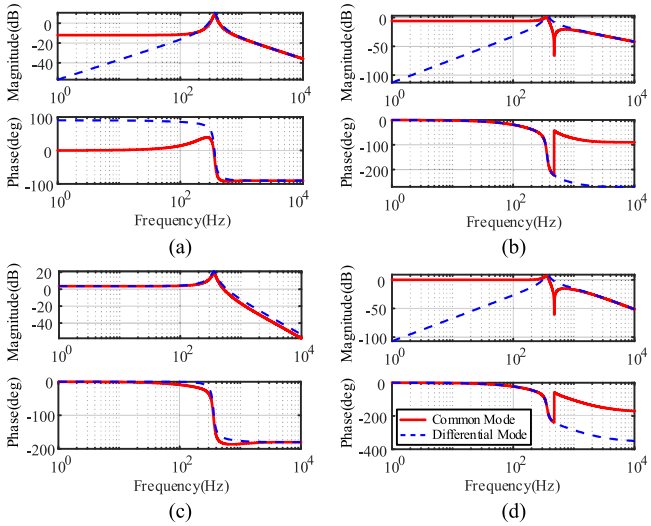

Fig. 9. Bode plots of the common mode and differential mode components on each state variables. (a) i_{L1}. (b) i_{Lf}. (c) v_{C1}. (d) v_{Cf}.

where f_{com0} and f_{dif0} are resonant frequencies under common mode and differential mode perturbation when R_{L} is relatively small, respectively. $f_{\mathrm{com}i,i=1,2}$ and $f_{\mathrm{dif}i,i=1,2}$ are resonant frequencies under common mode and differential mode perturbation when R_{L} is large, respectively.

In order to calculate the other additional resonant frequency, the circuit is assumed to work on that parallel resonant state. In this case, the impedance of L_1C_1 branch is infinity, i.e., the current through $R_{\mathrm{L}}L_{\mathrm{f}}C_{\mathrm{f}}$ branch is 0, so the $R_{\mathrm{L}}L_{\mathrm{f}}C_{\mathrm{f}}$ branch has two equal nodal voltages. The inductor L_1 is equivalently divided into two series connected inductors, as plotted in Fig. 8. The equivalent inductor $\frac{1}{2D_1'^2}L_1$ and capacitor C_1 are the cause of the parallel resonant, and the additional resonant frequency can be expressed as

$$f_{\mathrm{com3}} = \frac{\sqrt{2}D'_1}{2\pi\sqrt{L_1C_1}}. \tag{19}$$

With the circuit parameter values of the double-input Cuk–Buck converter given as $V_{\mathrm{in1}} = 10\,\mathrm{V}, V_{\mathrm{in2}} = 18\,\mathrm{V}, L_1 = 1\,\mathrm{mH}$, $L_{\mathrm{f}} = 1\,\mathrm{mH}$, $C_1 = 100\,\mu\mathrm{F}$, $C_{\mathrm{f}} = 47\,\mu\mathrm{F}$, $R_{\mathrm{L}} = 2\,\Omega$, and $f_{\mathrm{s}} = 20\,\mathrm{kHz}$. System simulation is performed by using the equivalent SPICE-based circuit, and the Bode plots of the common mode and differential mode power components on each state variables are obtained by injecting ac signal source with varying frequency, as depicted in Fig. 9, where the red solid line and blue dash line denote the common mode and differential mode components, respectively. If compared with the Bode plots of the common mode and differential mode components in Fig. 9, it can be found that the common mode component has the same resonant frequency as the differential mode one, and more surprisingly, the common mode component has one additional resonant frequency [see Fig. 9(b) and (d)]. These phenomena are consistent with the abovementioned analytical results.

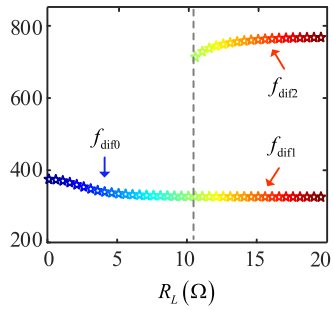

Fig. 10. Influence of load R_{L} on the resonant frequency.

The influence of the load R_{L} on the resonant frequency under differential mode perturbation is illustrated in Fig. 10. It can be seen that when R_{L} is relatively small, there exists a resonant frequency f_{dif0} under differential mode perturbation. Interestingly, as R_{L} increases, there are two resonant frequencies of the SPICE-based circuit, i.e., f_{dif1} and f_{dif2}. Additionally, the resonant frequencies are lower than the switching frequency. This is because the low frequency power flow under study usually plays a major role in system dynamics as well as stability. These results are in accordance with those analytical results in (16) and (17).

C. Under Power Mismatched Condition

In practice, as long as (10) is not satisfied, the power balance between the two input ports is broken. That is, the mismatched condition occurs. It is easy to find that the power mismatched condition can be divided into two parts, i.e., the power flow perturbation from port $1^{\#}$ is larger than that of port $2^{\#}$, i.e., $\hat{P}_1 > \hat{P}_2$ and the other is opposite, i.e., $\hat{P}_1 < \hat{P}_2$.

1) Common Mode Perturbation Analysis: It is worth mentioning that no matter $\hat{P}_1 > \hat{P}_2$ or $\hat{P}_1 < \hat{P}_2$, the power flow under common mode perturbation always keeps the same direction as the power matched condition. Therefore, the frequency characteristics in common mode perturbation will remain the same except that the amplitudes are different from each other.

2) Differential Mode Perturbation Analysis When $\hat{P}_1 > \hat{P}_2$: Under differential mode perturbation, once the power matched condition is broken, the equivalent circulating current is generated between the two input ports, and the frequency characteristics of the system state variables change essentially. When $\hat{P}_1 > \hat{P}_2$, the power flow perturbation of each source in Fig. 11 can be decomposed into

$$\begin{bmatrix} \hat{P}_1 \\ \hat{P}_2 \end{bmatrix} = \begin{bmatrix} 1 & 1 \\ 1 & -1 \end{bmatrix} \begin{bmatrix} \hat{P}_{\mathrm{dif}} \\ \hat{P}_{\mathrm{com}} \end{bmatrix} \tag{20}$$

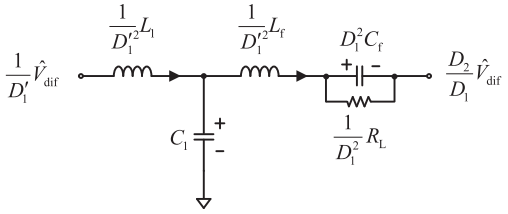

Fig. 11. Equivalent SPICE-based circuit under differential mode perturbation when power mismatch.

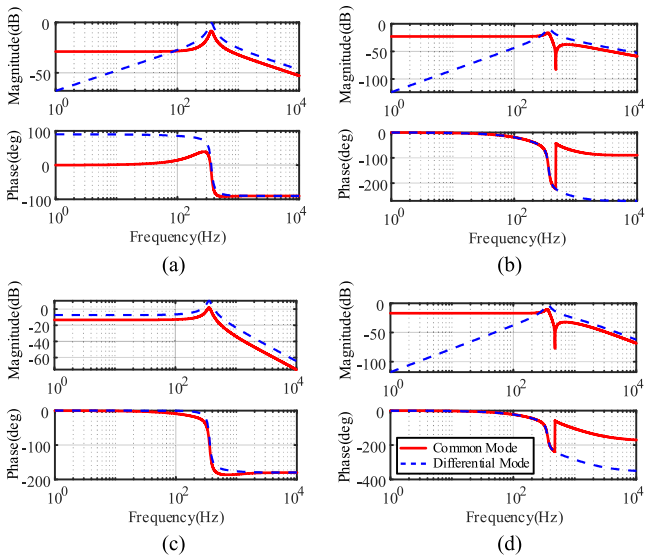

Fig. 12. Bode plots of differential mode perturbation for $\hat{P}_{\rm com}$ and $\hat{P}_{\rm dif}$ when $\hat{P}_{\rm dif} = 10\hat{P}_{\rm com}$. (a) i_{L1}. (b) i_{Lf}. (c) v_{C1}. (d) v_{Cf}.

where $\hat{P}_{\rm dif} = \frac{1}{2}(\hat{P}_1 + \hat{P}_2)$ has the same direction as the current of differential mode perturbation under power matched condition. $\hat{P}_{\rm com} = \frac{1}{2}(\hat{P}_1 - \hat{P}_2)$, which is the same direction as the current of differential mode perturbation under matched condition. Noted that $\hat{P}_1$ and $\hat{P}_2$ are in opposite directions. Furthermore, the relationship between the common mode and differential mode power flow perturbations and the common mode and differential mode voltage perturbations can be characterized as

$$\begin{bmatrix} \hat{P}_{\rm dif} \\ \hat{P}_{\rm com} \end{bmatrix} = \frac{1}{2} I_{Lf} \begin{bmatrix} \frac{D_1}{1-D_1} - D_2 & \frac{D_1}{1-D_1} + D_2 \\ \frac{D_1}{1-D_1} + D_2 & \frac{D_1}{1-D_1} - D_2 \end{bmatrix} \begin{bmatrix} \hat{V}_{\rm com} \\ \hat{V}_{\rm dif} \end{bmatrix}. \quad (21)$$

Therefore, for the differential mode perturbation under power mismatched condition, it can be regarded as the superposition of common mode perturbation $\hat{P}_{\rm com}$ and differential mode perturbation $\hat{P}_{\rm dif}$ under matched condition.

An example will be given to illustrate the mechanism of the superposition in general condition. Provided that $\hat{P}_{\rm dif} = 10\hat{P}_{\rm com}$, the Bode plots of differential mode perturbation for $\hat{P}_{\rm com}$ and $\hat{P}_{\rm dif}$ are shown in Fig. 12, where the red solid line and the blue dash line are $\hat{P}_{\rm com}$ and $\hat{P}_{\rm dif}$, respectively. It can be found that the common mode perturbation in Fig. 12 has the same shape as the common mode perturbation under matched condition in Fig. 9, but the amplitude is nearly 10 times smaller than that in Fig. 9. Since the general differential mode perturbation

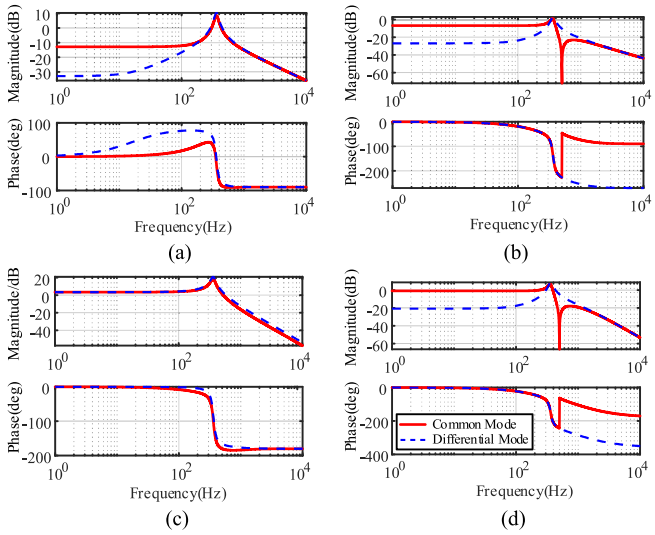

Fig. 13. Bode plots of common mode and differential mode perturbation when $\hat{P}_1 > \hat{P}_2$. (a) i_{L1}. (b) i_{Lf}. (c) v_{C1}. (d) v_{Cf}.

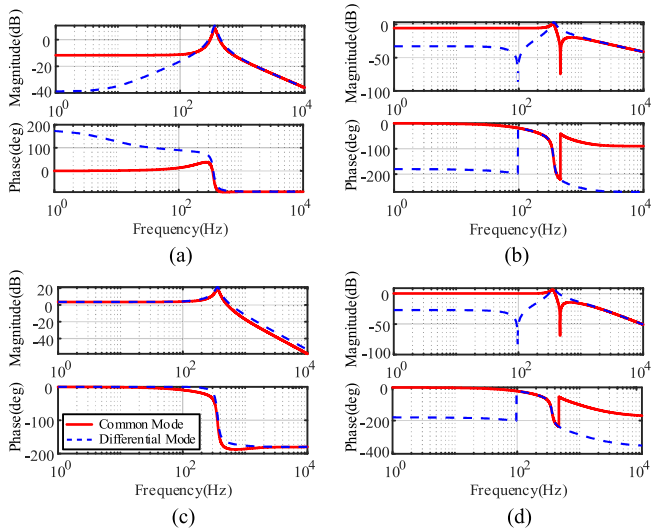

Fig. 14. Bode plots of common mode and differential mode perturbation when $\hat{P}_1 < \hat{P}_2$. (a) i_{L1}. (b) i_{Lf}. (c) v_{C1}. (d) v_{Cf}.

can be considered as the superposition of common mode and differential mode under matched condition in this case, the actual differential mode perturbation is approximately the maximum of the red solid line and the blue dash line in Fig. 12. And the Bode plots of common mode and differential mode perturbations are depicted in Fig. 13.

3) Differential Mode Perturbation Analysis When $\hat{P}_1 < \hat{P}_2$: Likewise, when $\hat{P}_1 < \hat{P}_2$, the differential mode perturbation can be performed with the decomposition method mentioned above. Noted that when $\hat{P}_1 < \hat{P}_2$, the direction of the common mode perturbation $\hat{P}_{\rm com}$ will reverse. Hence, in this case, the differential mode perturbation is obtained from the difference between $\hat{P}_{\rm com}$ and $\hat{P}_{\rm dif}$ under matched condition. And the Bode plots of common mode and differential mode perturbations are illustrated in Fig. 14.

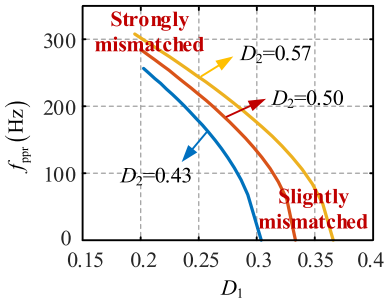

Fig. 15. $f_{\rm ppr}$ versus D_1 in different D_2.

Interestingly, when $\hat{P}_1 < \hat{P}_2$, the reverse direction of the common mode power flow perturbation $\hat{P}_{\rm com}$ causes one special phenomenon. That is, at a particular frequency, the amplitudes of $\hat{P}_{\rm com}$ and $\hat{P}_{\rm dif}$ under power matched condition are the same but the phases are opposite. Since the $\hat{P}_{\rm com}$ and $\hat{P}_{\rm dif}$ in $R_{\rm L}L_{\rm f}C_{\rm f}$ branch cancel each other, the gains of i_{Lf} and v_{Cf} are zero, i.e., a "pseudo" resonance happens, and the pseudo resonant frequency $f_{\rm ppr}$ is shown in the Bode plots of differential mode perturbation in this case [see Fig. 14(b) and (d)].

The variation of $f_{\rm ppr}$ with respect to D_1 and D_2 is depicts in Fig. 15. $f_{\rm ppr}$ gradually decreases with the increasing of D_1, and eventually disappears once D_1 makes the power matched condition valid. In addition, it can be observed that $f_{\rm ppr}$ monotonically increases with D_2. Noted that the lower right portion of Fig. 15 actually implies a slight mismatched condition and the upper left portion does a strong mismatched condition. Therefore, $f_{\rm ppr}$ is generally higher in power mismatched condition. That is, the pseudo resonant frequency can be a signal to show the extent of the power mismatched condition.

IV. Application to Frequency-Selective Decoupling Control

From the above-mentioned power flow coupling analysis, it follows that common mode perturbation analysis reveals the power flow coupling amongst input and output ports, whereas differential mode perturbation analysis does the power flow coupling between input ports. Thus, based on the common mode and differential mode decomposition, power flow coupling method analysis will be applied to frequency-selective decoupling control design, as an example.

The power management of MICs should not only ensure the input–output power flow balance, but also realize the input power distribution. For the double-input Cuk–Buck converter, assuming that the 1# port current is controlled by d_1 to manage the input power, and the output voltage is regulated by d_2 in order to assure the balance and distribution of system power.

The small-signal (6) can be rewritten as

$$\dot{\hat{\boldsymbol{x}}} = \boldsymbol{A}\hat{\boldsymbol{x}} + \boldsymbol{B}\hat{\boldsymbol{d}}. \tag{22}$$

By performing Laplace transform on (22), it yields

$$\hat{\boldsymbol{x}}(s) = (s\boldsymbol{I} - \boldsymbol{A})^{-1}\boldsymbol{B}\hat{\boldsymbol{d}}(s) = \boldsymbol{G}(s)\,\hat{\boldsymbol{d}}(s) \tag{23}$$

where $\boldsymbol{G}(s)$ is the transfer function matrix, and the transfer functions of $\hat{i}_{L1}$, $\hat{v}_{Cf}$ to $\hat{d}_1$, $\hat{d}_2$ are $G_{11}(s)$, $G_{12}(s)$, $G_{41}(s)$, and $G_{42}(s)$, respectively, as given below. Therefore, the control-output transfer function can be obtained

$$\begin{bmatrix}\hat{i}_{L1}\\ \hat{v}_{Cf}\end{bmatrix} = \begin{bmatrix}G_{11}(s) & G_{12}(s)\\ G_{41}(s) & G_{42}(s)\end{bmatrix}\begin{bmatrix}\hat{d}_1\\ \hat{d}_2\end{bmatrix} = \boldsymbol{G'}(s)\,\hat{\boldsymbol{d}}(s). \tag{24}$$

Evidently, neither $G_{12}(s)$ nor $G_{41}(s)$ is zero, so $\boldsymbol{G'}(s)$ is a nondiagonal matrix, which indicates that there is a coupling between $\hat{i}_{L1}$ and $\hat{v}_{Cf}$ so that the complexity of controller design increases. If the values of nondiagonal elements relative to

$$G_{11}(s) = \frac{C_1C_{\rm f}L_{\rm f}R_{\rm L}V_{\rm C1}s^3+[C_1V_{C1}+D'_1(I_{L1}+I_{Lf})R_{\rm L}C_{\rm f}]L_{\rm f}s^2+[(D_1C_{\rm f}+C_1)R_{\rm L}V_{C1}+D'_1(I_{\rm L1}+I_{\rm Lf})L_{\rm f}]s+D'_1(I_{L1}+I_{Lf})R_{\rm L}+D_1V_{C1}}{C_1C_{\rm f}L_1L_{\rm f}R_{\rm L}s^4+C_1L_1L_{\rm f}s^3+(C_1L_1+C_{\rm f}L_{\rm f}-2C_{\rm f}D_1L_{\rm f}+C_{\rm f}{D_1}^2L_1+C_{\rm f}{D_1}^2L_{\rm f})R_{\rm L}s^2+(L_{\rm f}+{D_1}^2L_1+{D_1}^2L_{\rm f}-2D_1L_{\rm f})s+R_{\rm L}D_1'^2}$$

$$G_{12}(s) = -\frac{R_{\rm L}C_{\rm f}D_1D'_1V_{\rm in2}s+D_1D'_1V_{\rm in2}}{C_1C_{\rm f}L_1L_{\rm f}R_{\rm L}s^4+C_1L_1L_{\rm f}s^3+(C_1L_1+C_{\rm f}L_{\rm f}-2C_{\rm f}D_1L_{\rm f}+C_{\rm f}{D_1}^2L_1+C_{\rm f}{D_1}^2L_{\rm f})R_{\rm L}s^2+(L_{\rm f}+{D_1}^2L_1+{D_1}^2L_{\rm f}-2D_1L_{\rm f})s+R_{\rm L}{D'}^2{}_1}$$

$$G_{41}(s) = \frac{C_1L_1R_{\rm L}V_{\rm C1}s^2-(I_{L1}+I_{Lf})D_1R_{\rm L}L_1s+D'_1R_{\rm L}V_{C1}}{C_1C_{\rm f}L_1L_{\rm f}R_{\rm L}s^4+C_1L_1L_{\rm f}s^3+(C_1L_1+C_{\rm f}L_{\rm f}-2C_{\rm f}D_1L_{\rm f}+C_{\rm f}{D_1}^2L_1+C_{\rm f}{D_1}^2L_{\rm f})R_{\rm L}s^2+(L_{\rm f}+{D_1}^2L_1+{D_1}^2L_{\rm f}-2D_1L_{\rm f})s+R_{\rm L}D_1'^2}$$

$$G_{42}(s) = \frac{R_{\rm L}C_1L_1V_{\rm in2}s^2+({D_1}^2-2D_1+1)R_{\rm L}V_{\rm in2}}{C_1C_{\rm f}L_1L_{\rm f}R_{\rm L}s^4+C_1L_1L_{\rm f}s^3+(C_1L_1+C_{\rm f}L_{\rm f}-2C_{\rm f}D_1L_{\rm f}+C_{\rm f}{D_1}^2L_1+C_{\rm f}{D_1}^2L_{\rm f})R_{\rm L}s^2+(L_{\rm f}+{D_1}^2L_1+{D_1}^2L_{\rm f}-2D_1L_{\rm f})s+R_{\rm L}D_1'^2}$$

diagonal elements, i.e., $G_{12}(s)/G_{11}(s)$ and $G_{41}(s)/G_{42}(s)$ can be reduced, $\boldsymbol{G'}(s)$ will be or be approximately a diagonal matrix. Accordingly, the coupling system can be decoupled into two single-input single-output systems, which results in realizing the relatively independent control of the system state variables.

The actual power flow perturbation is the combination of common mode and differential mode components. It can be observed from Figs. 9, 13, and 14 that the differential mode perturbation exhibits more external dominant characteristics, which plays a leading role in the power flow coupling between ports of the double-input converter. Moreover, the coupling degree at the resonant point increases rapidly, which causes drastic variations in the direction or amplitude of some power flow. Taking $R_{\mathrm{L}} = 2\,\Omega$ under power matched condition as an example, when the input perturbation frequency f_{d} is at the differential mode resonant frequency f_{dif0} of 375 Hz

$$\begin{aligned}\hat{i}_{L1} &= (-39.523 - 116.43\mathrm{i})\,\hat{d}_1 - (18.030 + 4.0719\mathrm{i})\,\hat{d}_2\\ \hat{v}_{C\mathrm{f}} &= (-15.4555 + 87.6373\mathrm{i})\,\hat{d}_1 + (17.9831 + 0.0746\mathrm{i})\,\hat{d}_2.\end{aligned} \tag{25}$$

As f_{d} decreases to 225 Hz

$$\begin{aligned}\hat{i}_{L1} &= (35.4584 - 3.9305\mathrm{i})\,\hat{d}_1 - (4.5374 + 4.1437\mathrm{i})\,\hat{d}_2\\ \hat{v}_{C\mathrm{f}} &= (0.1154 - 27.7526\mathrm{i})\,\hat{d}_1 + (8.6235 - 10.2673\mathrm{i})\,\hat{d}_2.\end{aligned} \tag{26}$$

Similarly, when f_{d} increases to 1125 Hz

$$\begin{aligned}\hat{i}_{L1} &= (-1.8877 - 2.2302\mathrm{i})\,\hat{d}_1 + (-0.0324 + 0.1396\mathrm{i})\,\hat{d}_2\\ \hat{v}_{C\mathrm{f}} &= (0.2705 - 4.2392\mathrm{i})\,\hat{d}_1 - (1.7143 + 4.5785\mathrm{i})\,\hat{d}_2.\end{aligned} \tag{27}$$

It can be readily found that when f_{d} decreases from f_{dif0} to 225 Hz (or increases to 1125 Hz), the values of $G_{12}(s)$ relative to $G_{11}(s)$ and $G_{41}(s)$ relative to $G_{42}(s)$ are significantly reduced, the diagonal dominance of $\boldsymbol{G'}(s)$ is enhanced. This implies that the coupling degree of the double-input converter system is weakened.

To weaken or eliminate the power flow coupling amongst three ports, the frequency-selective decoupling transfer function is defined as

$$G_{\mathrm{F}}(s) = \frac{s^2 + {\omega_{\mathrm{d}}}^2}{s^2 + Bs + {\omega_{\mathrm{d}}}^2} \tag{28}$$

where $\omega_{\mathrm{d}} = 2\pi f_{\mathrm{dif0}}$ is the center frequency, and B is the stop-band width.

The control-output transfer function can be rewritten as

$$\begin{aligned}\begin{bmatrix}\hat{i}_{L1}\\ \hat{v}_{C\mathrm{f}}\end{bmatrix} &= G_{\mathrm{F}}(s)\begin{bmatrix}G_{11}(s) & G_{12}(s)\\ G_{41}(s) & G_{42}(s)\end{bmatrix}\begin{bmatrix}\hat{d}_1\\ \hat{d}_2\end{bmatrix}\\ &= \begin{bmatrix}G^*_{11}(s) & G^*_{12}(s)\\ G^*_{41}(s) & G^*_{42}(s)\end{bmatrix}\begin{bmatrix}\hat{d}_1\\ \hat{d}_2\end{bmatrix}.\end{aligned} \tag{29}$$

To investigate the coupling effect between $\hat{i}_{L1}$ and $\hat{d}_1$ as well as $\hat{v}_{C\mathrm{f}}$ and $\hat{d}_2$ before and after frequency-selective decoupling control, the frequency characteristic curves of nondiagonal elements in $\boldsymbol{G'}(s)$ are depicted in Fig. 16. The larger the gains of $G_{12}(s)$ and $G_{41}(s)$ at the resonant frequency, the stronger the coupling effect between $\hat{i}_{L1}$ and $\hat{d}_1$ as well as $\hat{v}_{C\mathrm{f}}$ and $\hat{d}_2$. After

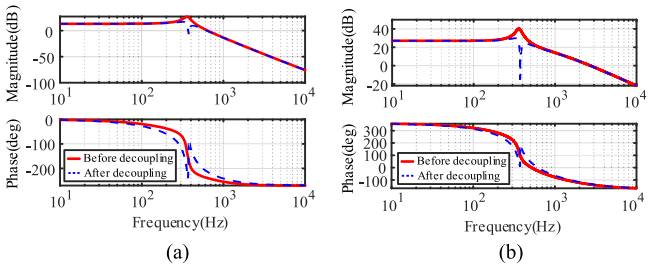

Fig. 16. Bode plots before and after decoupling. (a)$G_{12}(s)$. (b)$G_{41}(s)$.

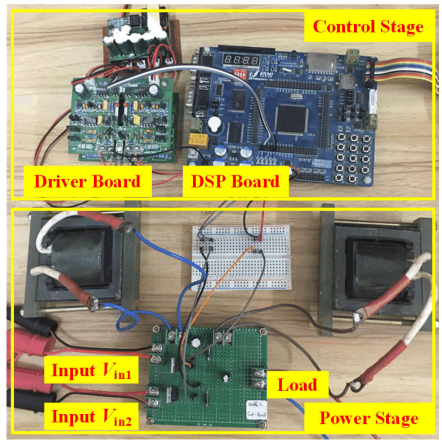

Fig. 17. Photograph of the experimental circuit.

frequency-selective decoupling control, it is clear that the gains of $G^*_{12}(s)$ and $G^*_{41}(s)$ at the resonant frequency are extremely reduced, i.e., the coupling effect between $\hat{i}_{L1}$ and $\hat{d}_1$ as well as $\hat{v}_{C\mathrm{f}}$ and $\hat{d}_2$ are weakened.

Since the input perturbation signals near the differential mode resonant frequency are filtered through the frequency-selective decoupling unit, the value of $G_{11}(s)$ and $G_{42}(s)$ are much smaller than those of $G^*_{11}(s)$ and $G^*_{42}(s)$, i.e., the coupling degrees are weakened. That is, the control decoupling from output to input is approximately realized. The original coupling system is approximately decoupled into two independent single-input single-output control systems, namely

$$\begin{bmatrix}\hat{i}_{L1}\\ \hat{v}_{C\mathrm{f}}\end{bmatrix} = \begin{bmatrix}G^*_{11}(s) & 0\\ 0 & G^*_{42}(s)\end{bmatrix}\begin{bmatrix}\hat{d}_1\\ \hat{d}_2\end{bmatrix}. \tag{30}$$

V. Experimental Results

Since we are concerned about the port coupling effect of the converter system, we may impose external perturbation on state variables to explore the frequency response characteristics, especially the behavior in resonant points so that the power flow coupling analysis will be verified. For ease of implementation, continuous sinusoidal perturbations with different frequencies and constant amplitudes are injected into the duty cycles.

For verifying the abovementioned theoretical and simulation results, an experimental prototype of the double-input Cuk–Buck converter is constructed, as shown in Fig. 17. The parameter and component values are listed in Table I. In this experiment, the MOSFETs are IRF540, the power diodes are FR207, and the

TABLE I
CIRCUIT PARAMETERS

Parameters	Values
Input voltages V_{in1}, V_{in2}	10V, 18V
Inductances L_1, L_2	1mH, 1mH
Capacitances C_1, C_f	100μF, 47μF
Load resistance R_L	10Ω
Switching frequency f_s	20kHz

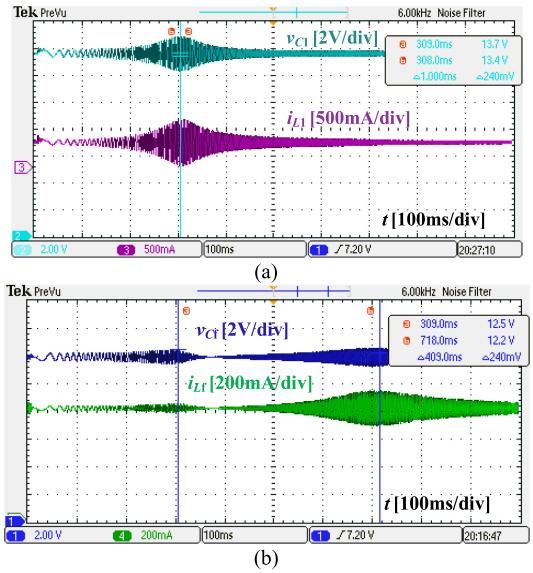

Fig. 18. Amplitude frequency response waveforms with $\hat{d}_1$ when $R_L = 15\,\Omega$. (a) i_{L1} and v_{C1}. (b) i_{Lf} and v_{Cf}.

digital signal controller TMS320F28335 has been chosen to generate the stable PWM signal.

The amplitudes of the response waveform of the corresponding output state variables are different because the system has different gains to signals of different perturbation frequencies. Thus, the amplitude variation of the output state variable response waveform reveals the amplitude frequency characteristics of the converter system. Since the changing process of state variables can be displayed, the experimental results are intuitive and clear.

Provided that the system is working in power matched condition, i.e., the steady-state duty cycles are $D_1 = 0.33$ and $D_2 = 0.5$, respectively. By injecting continuous sinusoidal perturbations with 3% amplitude into D_1, and the frequency increases from 1 Hz to 1000 Hz within 1s, the amplitude frequency response waveforms of i_{L1}, i_{Lf}, v_{C1}, and v_{Cf} are depicted in Fig. 18. It is clear that the amplitude of the waveform response of all the $G^*_{41}(s)$state variable is large when the injected perturbation frequency is about 309 Hz. In particular, the maximum response amplitude of i_{L1} reaches 550 mA, and the response amplitude of v_{C1} increases to nearly 13.7 V. Obviously, this injected perturbation frequency of 309 Hz is just the resonant frequency f_{dif1} (i.e., 309 Hz) of the system. Fig. 19 further shows the response waveforms of v_{Cf} at the perturbation frequencies of 310 Hz and 340 Hz, respectively. It can be found that the response amplitude of v_{Cf} at the perturbation frequency of

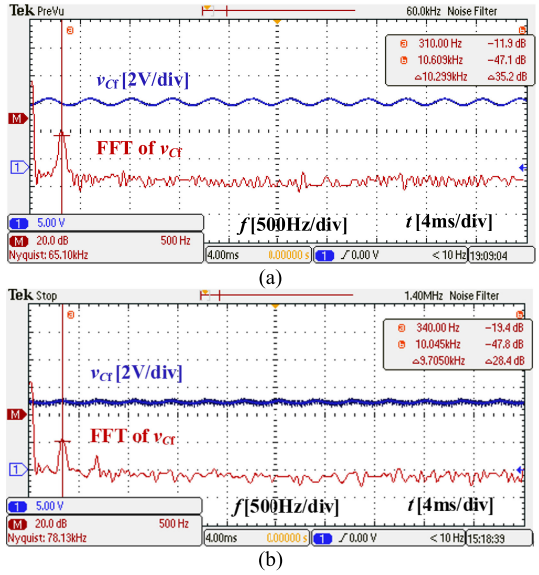

Fig. 19. Response waveforms of v_{Cf} with $\hat{d}_1$ at different frequencies. (a) 310 Hz. (b) 340 Hz.

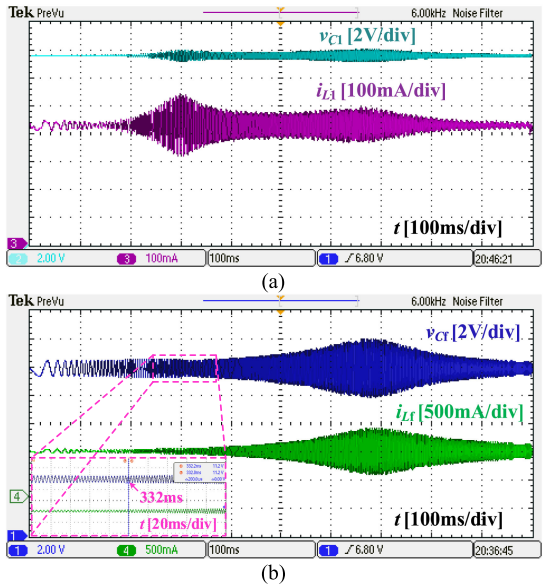

Fig. 20. Amplitude frequency response waveforms with $\hat{d}_2$ when $R_L = 15\,\Omega$. (a) i_{L1} and v_{C1}. (b) i_{Lf} and v_{Cf}.

310 Hz is much larger than that of 340 Hz. Strangely, there exists a large response amplitude near the perturbation frequency of 718 Hz besides the perturbation frequency around 309 Hz [see Fig. 18(b)]. It can be recognized that the response amplitudes of i_{Lf} and v_{Cf} increase significantly and peak at the perturbation frequency of 718 Hz. These indicate that another new resonant frequency f_{dif2} (i.e., 718 Hz) has been found in this system.

Likewise, when continuous sinusoidal perturbations with frequency from 0 Hz to 1000 Hz are added to D_2, the amplitude frequency response waveforms of all the state variables are illustrated in Fig. 20. It can be seen that the response amplitudes of all the state variables reach a large value when the injected perturbation frequency is 309 Hz or 718 Hz. It is demonstrated

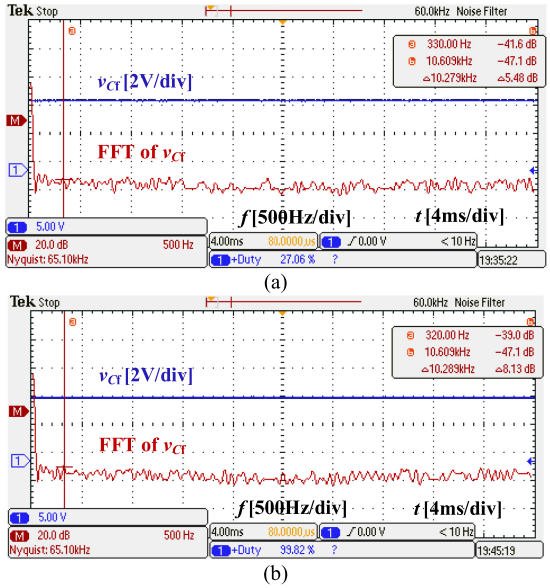

Fig. 21. Response waveforms of v_{Cf} with $\hat{d}_2$ at different frequencies. (a) 330 Hz. (b) 340 Hz.

that there are two resonant frequencies of 309 Hz and 718 Hz in the system. Interestingly, there is an unobtrusive valley in the response amplitude of v_{Cf} at around 332 Hz [see Fig. 20(b)]. Fig. 21 depicts the response waveform of v_{Cf} under the perturbation frequency of 330 Hz and 340 Hz, respectively. We can see that the response amplitude of v_{Cf} at the perturbation frequency of 330 Hz is slightly smaller than the case of 340 Hz. It indicates the existence of the resonant frequency $f_{\mathrm{com3}}/\sqrt{2}$ (i.e., 332 Hz) in the system.

Consequently, these experimental results are in accordance with those theoretical and numerical results, which is helpful in understanding the power flow coupling effect of the double-input Cuk–Buck converter.

VI. Conclusion

In this article, the SPICE-based circuit analysis of power flow coupling in the double-input Cuk–Buck converter is performed and the corresponding application of frequency-selective decoupling is proposed. First, to observe power flow coupling path intuitively from the view of physical circuit, an equivalent SPICE-based circuit is derived from the small-signal averaged model including some abstract mathematical expressions. Second, the power flow decomposition is proposed from the perspective of common mode and differential mode perturbation of the input power so that power flow coupling in MICs can be surely unveiled. Specifically, the power flow coupling amongst input and output ports is revealed by common mode perturbation analysis, while the power flow coupling between input ports is indicated by differential mode perturbation analysis. It is further revealed that the differential mode perturbation plays a dominant role in the power flow coupling between ports. Furthermore, based on the equivalent SPICE-based circuit, the explanation of circuit knowledge is provided for power flow coupling effect by performing the common mode and differential mode power flow decomposition of input ports. The coupling degree of the energy storage elements at the resonant frequency is deepened, and the direction or amplitude of the power flow changes drastically. Meanwhile, the analytical expressions of resonant frequencies with respect to circuit parameters are obtained. More importantly, the mechanism of the pseudo resonant phenomenon has been pointed out to be the result of counteract effect of the common mode and differential mode components in power mismatched condition, and it follows that the pseudo resonant frequency increases with the extent of the power mismatched. Then, the application of the frequency-selective decoupling is given, which filters the input perturbation signals near the differential mode resonant frequency so that to weaken or eliminate the coupling between ports. Finally, experimental results have been presented to verify the validity of the abovementioned analysis. These results are important for the controller optimization and engineering application of MICs.

References

[1] M. C. Mira, Z. Zhang, A. Knott, and M. A. Andersen, "Analysis, design, modeling, and control of an interleaved-boost full-bridge three-port converter for hybrid renewable energy systems," *IEEE Trans. Power Electron.*, vol. 32, no. 2, pp. 1138–1155, Feb. 2017.

[2] H. Zhang, D. C. Dong, M. Jing, W. Liu, and F. Zheng, "Topology derivation of multiple-port DC-DC converters based on voltage-type ports," *IEEE Trans. Ind. Electron.*, to be published, doi: 10.1109/TIE.2021.3078389.

[3] A. K. Bhattacharjee, N. Kutkut, and I. Batarseh, "Review of multiport converters for solar and energy storage integration," *IEEE Trans. Power Electron.*, vol. 34, no. 2, pp. 1431–1445, Feb. 2019.

[4] Y. Sato, M. Uno, and H. Nagata, "Nonisolated multiport converters based on integration of PWM converter and phase-shift-switched capacitor converter," *IEEE Trans. Power Electron.*, vol. 35, no. 1, pp. 455–470, Jan. 2020.

[5] R. Faraji and H. Farzanehfard, "Soft-switched nonisolated high step-up three-port DC-DC converter for hybrid energy systems," *IEEE Trans. Power Electron.*, vol. 33, no. 12, pp. 10101–10111, Dec. 2018.

[6] W. Liu, H. Zhang, D. C. Dong, W. Liu, and H. H. Ding, "Multi-harmonic interaction and stability analysis of two-stage double-input buck inverter," *IEEE J. Emerg. Sel. Topics Power Electron.*, to be published, doi: 10.1109/JESTPE.2021.3113119.

[7] X. L. Xiong and X. B. Ruan, "Non-smooth bifurcation analysis of multi-structure multi-operating-mode power electronics systems for applications with renewable energy sources," *IEEE Trans. Circuits Syst. I, Reg. Papers*, vol. 66, no. 3, pp. 487–491, Mar. 2019.

[8] O. L. Lapeña, "Time-division multiplexing control of multi-input converters for low-power solar energy harvesters," *IEEE Trans. Ind. Electron.*, vol. 65, no. 12, pp. 9668–9676, Dec. 2018.

[9] B. Wang, X. Zhang, J. Ye, and H. B. Gooi, "Deadbeat control for a single-inductor multiple-input multiple-output DC–DC converter," *IEEE Trans. Power Electron.*, vol. 34, no. 2, pp. 1914–1924, Feb. 2019.

[10] H. Zhang, D. C. Dong, W. Liu, H. Ren, and F. Zheng, "Systematic synthesis of multiple-input and multiple-output DC-DC converters for non-isolated applications," *IEEE J. Emerg. Sel. Topics Power Electron.*, to be published, doi: 10.1109/JESTPE.2021.3118797.

[11] W. H. Li, C. Xu, H. Z. Luo, Y. H. Hu, X. N. He, and C. L. Xia, "Decoupling-controlled triport composited DC/DC converter for multiple energy interface," *IEEE Trans. Ind. Electron.*, vol. 62, no. 7, pp. 4504–4513, Jul. 2015.

[12] Z. J. Qian, O. Abdel Rahman, and I. Batarseh, "An integrated four-port DC/DC converter for renewable energy applications," *IEEE Trans. Power Electron.*, vol. 25, no. 7, pp. 1877–1887, Jul. 2010.

[13] Z. J. Qian, O. Abdel Rahman, H. Al Atrash, and I. Batarseh, "Modeling and control of three-port DC/DC converter interface for satellite applications," *IEEE Trans. Power Electron.*, vol. 25, no. 3, pp. 637–649, Mar. 2010.

[14] Y. M. Chen, A. Q. Huang, and X. W. Yu, "A high step-up three-port DC-DC converter for stand-alone PV/battery power systems," *IEEE Trans. Power Electron.*, vol. 28, no. 11, pp. 5049–5062, Nov. 2013.

[15] W. Jiang and B. Fahimi, "Multiport power electronic interface—Concept, modeling, and design," *IEEE Trans. Power Electron.*, vol. 26, no. 7, pp. 1890–1900, Jul. 2011.
[16] D. S. Yang, M. Yang, and X. B. Ruan, "One-cycle control for a double-input DC/DC converter," *IEEE Trans. Power Electron.*, vol. 27, no. 11, pp. 4646–4655, Nov. 2012.
[17] H. Zhang, S. Dong, W. M. Guan, C. Z. Yi, and B. He, "Adaptive control of fast-scale bifurcation in peak current controlled buck-boost inverter via one-cycle compensation," *Int. J. Bifurcation Chaos*, vol. 26, no. 12, 2016, Art. no. 1650201.
[18] R. Ahmadi, H. Zargarzadeh, and M. Ferdowsi, "Nonlinear power sharing controller for a double-input H-bridge-based buckboost–buckboost converter," *IEEE Trans. Power Electron.*, vol. 28, no. 5, pp. 2402–2414, May 2013.
[19] C. N. Onwuchekwa and A. Kwasinski, "A modified-time-sharing switching technique for multiple-input DC-DC converters," *IEEE Trans. Power Electron.*, vol. 27, no. 11, pp. 4492–4502, Nov. 2012.
[20] R. R. Ahrabi, H. Ardi, M. Elmi, and A. Ajami, "A novel step-up multiinput DC-DC converter for hybrid electric vehicles application," *IEEE Trans. Power Electron.*, vol. 32, no. 5, pp. 3549–3561, May 2017.
[21] F. Nejabatkhah, S. Danyali, S. H. Hosseini, M. Sabahi, and S. M. Niapour, "Modeling and control of a new three-input DC-DC boost converter for hybrid PV/FC/battery power system," *IEEE Trans. Power Electron.*, vol. 27, no. 5, pp. 2309–2324, May 2012.
[22] R. B. Ridley, "A new, continuous-time model for current-mode control (power convertors)," *IEEE Trans. Power Electron.*, vol. 6, no. 2, pp. 271–280, Apr. 1991.
[23] I. Stevanovic, S. Skibin, M. Masti, and M. Laitinen, "Behavioral modeling of chokes for EMI simulations in power electronics," *IEEE Trans. Power Electron.*, vol. 28, no. 2, pp. 695–705, Feb. 2013.
[24] T. Meng, H. Q. Ben, Y. L. Song, and C. Y. Li, "Analysis and suppression of the circulating current influence in the input-series auxiliary power supply for high-input-voltage applications," *IEEE Trans. Power Electron.*, vol. 34, no. 7, pp. 6533–6543, Jul. 2019.
[25] J. W. Moon, C. S. Kim, J. W. Park, D. W. Kang, and J. M. Kim, "Circulating current control in MMC under the unbalanced voltage," *IEEE Trans. Power Del.*, vol. 28, no. 3, pp. 1952–1959, Jul. 2013.
[26] T. Younis, P. Mattavelli, I. Toigo, and M. Corradin, "Three-phase modular multilevel converter with optimized capacitor sizing for low voltage applications," *IEEE Trans. Power Electron.*, vol. 36, no. 12, pp. 13930–13943, Dec. 2021.
[27] J. Freytes *et al.*, "Improving small-signal stability of an MMC with CCSC by control of the internally stored energy," *IEEE Trans. Power Del.*, vol. 33, no. 1, pp. 429–439, Feb. 2018.
[28] F. Corti, A. Reatti, E. Cardeli, A. Faba, and H. Rimal, "Improved spice simulation of dynamic core losses for ferrites with nonuniform field and its experimental validation," *IEEE Trans. Ind. Electron.*, vol. 68, no. 12, pp. 12069–12078, Dec. 2021, doi: 10.1109/TIE.2020.3044783.
[29] X. L. Li and Z. W. Du, "SPICE model for analyzing EMS responses of multilayer PCBs with nonlinear loads," in *Proc. IEEE 5th Int. Symp. Electromagn. Compat.*, EMC-Beijing, 2017, pp. 1–4, doi: 10.1109/EMC-B.2017.8260469.
[30] E. Locorotondo, L. Pugi, F. Corti, and L. Becchi, and F. Grasso, "Analytical model of power MOSFET switching losses due to parasitic components," in *Proc. IEEE 5th Int. Forum Res. Technol. Soc. Ind.*, 2019, pp. 331–336, doi: 10.1109/RTSI.2019.8895562.

Hao Zhang (Member, IEEE) was born in Shaanxi, China, in 1973. He received the B.E. degree from the Xi'an University of Science and Technology, Xi'an, China, in 1996, the M.Sc. degree from the Xi'an University of Technology, Xi'an, China, in 2002, and the Ph.D. (Hons.) degree in electrical engineering from Xi'an Jiaotong University, Xi'an, China, in 2005.

From December 2004 to June 2005, he was a Research Assistant with Hong Kong Polytechnic University, Hong Kong. Since 2007, he has been an Associate Professor with the School of Electrical Engineering, Xi'an Jiaotong University. From 2010 to 2011, he was a Visiting Professor with the Center for Power Electronics Systems, Virginia Tech, Blacksburg, VA, USA. His research interests include power electronics and its application to renewable energy generation.

Jiao Gao was born in Anhui, China, in 1997. She received the B.S. degree in smart grid information engineering from the Hefei University of Technology, Hefei, China, in 2019. She is currently working toward the M.S. degree in electrical engineering with the School of Electrical Engineering, Xi'an Jiaotong University, Xi'an, China.

Her research interests include modeling and dynamical analysis of power converters.

Chuanzhi Yi received the B.S. and M.S. degrees in electronic engineering from Xi'an Jiaotong University, Xi'an, China, in 2015 and 2018, respectively.

From 2018, he was employed by Bosch Automotive Product (Suzhou) Co., Ltd., as an Electronics Engineer. While there, he participated in the development of an high voltage motor drive for hybrid electric vehicle. His current research interests include SiC driver design, sensor-less motor control, and compact dc–dc converter.

Dachu Dong was born in Zhejiang Province, China, in 1997. He received the B.S. degree from Chongqing University, Chongqing, China, in 2018, and the M.S. degree from the School of Electrical Engineering, Xi'an Jiaotong University, Xi'an, China, in 2021, both in electrical engineering.

He is currently with the Hangzhou Power Supply Company of State Grid Zhejiang Electric Power Company, Ltd., Hangzhou, China. His research interests include topologies and modeling of power converters for renewable energy applications.

Feng Zheng (Member, IEEE) received the B.S., M.S., and Ph.D. degrees in electrical engineering from Xi'an Jiaotong University, Xi'an, China, in 1993, 2004, and 2008, respectively.

In 2008, he was with the School of Electrical and Mechanical Engineering, Xidian University, Xi'an, China. From 2010 to 2011, he was with the Center for Power Electronics Systems at Virginia Tech, Blacksburg, as a Postdoctor. He then came back to Xidian University, where he is currently an Associate Professor. His research interests include low voltage level, high power density dc–dc converters, and integrated magnetics.